Chemical Geology 592 (2022) 120687

Contents lists available at ScienceDirect

Chemical Geology

journal homepage: www.elsevier.com/locate/chemgeo

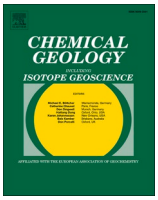

Dissolution of periodic arrays of grains: Upscaling of pore-scale simulations with fast reactions

Liang Yu [a], Piotr Szymczak [b], Anthony J.C. Ladd [a,*]

[a] Chemical Engineering, University of Florida, 1006 Center Drive, Gainesville, FL 32611-6005, United States
[b] Institute of Theoretical Physics, Faculty of Physics, University of Warsaw, Pasteura 5, 02-093, Warsaw, Poland

ARTICLE INFO

Editor: Karen Johannesson

Keywords:
Upscaling
Dissolution
Porous materials

ABSTRACT

Upscaling methods are frequently used to derive transport equations at the macroscopic scale from more fundamental equations formulated at the pore scale. These methods typically give a suitable structure for the macroscopic equations and can also provide explicit expressions for the constitutive parameters, such as permeability and dispersion coefficients. Introducing chemical reactions complicates upscaling in at least two important ways. First, the interplay between chemical reactions and transport processes introduces a new length scale, which can be much smaller than the convective or dispersive length scales. A small reactive length scale breaks one of the key assumptions in upscaling; that there is a significant separation in length between the pore-scale and macro-scale processes. The second complication is that if reactions take place at mineral surfaces (dissolution or precipitation) then the pore space itself is evolving in time. In this paper we suggest ways in which these difficulties can be approached, based on analysis of pore-scale simulation data. First, we noticed that the concentration field in successive unit cells has an almost identical spatial variation, with a single scaling factor for each unit cell that is proportional to the incoming reactant flux. Using pore-scale simulations to determine the mass transfer coefficient in a few unit cells, we can calculate the concentration field in the whole domain, even when dissolution is entirely transport limited. Second, we have noticed a time-dependent mapping of the grain shapes from different unit cells. From these observations, we can deduce constitutive relations where the only time-varying parameter is the porosity. We show that a model based on these ideas can quantitatively account for the pore-scale simulation data.

1. Introduction

Dissolution at the pore scale is described by the time evolution of the mineral fluid interfaces, which we denote collectively as $S(t)$. Since there is a large separation of time scales between the motion of the interface and the transport of mineral ions, the velocity and concentration fields are not explicitly time dependent, but are slaved to $S(t)$ (Lichtner, 1988; Phillips, 1990). The evolution of the system from a given initial condition is then determined by a small number of independently measurable parameters: fluid viscosity, ion diffusion coefficients, and surface reaction rates. Pore-scale data can be obtained on a limited scale from a variety of numerical simulation methods (Molins et al., 2020; Ladd and Szymczak, 2021). The problem investigated here is how to best utilize this information in cases where the dissolution is limited by the transport of ions to the mineral, rather than the kinetics of the surface reactions.

The geometric properties of a porous matrix introduce at least two length scales: the size of the pores and the dimensions of the system (Brenner, 1980; Whitaker, 1986; Auriault and Adler, 1995). Upscaling attempts to take information determined at the pore scale and use it to formulate equations at much larger scales, which nevertheless incorporate the pore-scale properties. However, in reactive transport this is not simply a matter of geometry, because chemical processes introduce their own length scales as well. Reactant is consumed by the porous matrix, so the concentration decays over some penetration length scale l_p, which varies with fluid velocity and surface reaction rate from millimeters to kilometers (Szymczak and Ladd, 2013). The dissolution rate of the solid is a combination of surface reaction, transport of reactant across the boundary layers around the grains, and the penetration of ions into the matrix. In this paper we will focus on upscaling transport-limited dissolution and therefore assume that the surface reaction is instantaneous.

* Corresponding author.
E-mail address: tladd@che.ufl.edu (A.J.C. Ladd).

https://doi.org/10.1016/j.chemgeo.2021.120687
Received 4 October 2021; Received in revised form 11 December 2021; Accepted 16 December 2021
Available online 21 December 2021

Averaging (or homogenization) methods provide an upscaled description of the evolution of the system (Brenner, 1980; Whitaker, 1986) by assuming the porous matrix is made up of periodic replicas of an underlying unit cell or "Representative Elementary Volume" (REV). Macroscopic equations are derived by averaging the fields over the individual unit cells (Brenner, 1980; Whitaker, 1986; Quintard and Whitaker, 1994a) or by a multiscale expansion of the fields (Auriault and Adler, 1995; Battiato and Tartakovsky, 2011). In either case, constitutive models can be obtained from closures at the pore scale (Quintard and Whitaker, 1994b; Golfier et al., 2002; Guo et al., 2016). Repeated upscaling can be used to homogenize heterogeneities occurring at scales larger than the individual pores (Golfier et al., 2004, 2006; Mehmani et al., 2012; Guo et al., 2021). Upscaling of reactive flows (Li et al., 2006; Lichtner and Kang, 2007) show that a multiscale continuum model is frequently necessary to capture the range of pore-scale heterogeneities.

When surface reactions are sufficiently fast, the solution of aqueous ions is in chemical equilibrium with the mineral (Lichtner, 1988), a condition that is met when the reaction rate constant tends to infinity. More precisely, we require that the combination $H = D\,ks/u_0^2 \gg 1$ (Szymczak and Ladd, 2013); here k is the rate constant (in m/s), s the reactive surface area (in m^{-1}), D the diffusion coefficient, and u_0 the mean flow velocity. The condition $H \gg 1$ can be represented by a Dirichlet boundary condition on the concentration field at the mineral-fluid interface. In this work we take $c = 0$, corresponding to the complete consumption of reactant by the mineral. However, although there is no chemical hindrance, dissolution is limited by the diffusive flux across the concentration boundary layer around the grains. Approximations to the high Damköhler limit can arise in geotechnical applications such as sequestration (Elkhoury et al., 2013; García-Ríos et al., 2015), and also in natural systems when the flow rate is sufficiently small that transport of reactants is the rate-limiting step (Lichtner, 1988). One observable characteristic of transport-limited reactions, is a sharp interface between different mineral phases (Lake et al., 2002; Szymczak and Ladd, 2013), which is frequently observed in natural rock formations (Shalev et al., 2006; Beinlich et al., 2012; Minde et al., 2020; Koeshidayatullah et al., 2021).

When the reaction rate is high ($H \gg 1$) the concentration field decays on the pore scale rather than the macroscopic scale. A multiscale analysis of homogenization (Battiato and Tartakovsky, 2011) reveals that a small Damköhler number $Da_{II} = kL/D \ll 1$ is necessary to maintain the separation of scales between the REV and the macroscopic length L. Similar restrictions were found in an analysis of reactive transport in parabolic flows (Mikelić et al., 2006). The purpose of the present paper is to investigate an alternative method of upscaling, which preserves the discrete nature of the individual REV and tracks the evolution of concentration fluxes rather than the field itself. The underlying idea is that an REV (cell n) is supplied with a flux of reactant J_{n-1}, and a certain fraction $\alpha_n J_{n-1}$ is absorbed by reactions with the solid surface. The outlet flux $J_n = (1 - \alpha_n)J_{n-1}$ becomes the inlet flux to the next cell $(n + 1)$, so that the rate of dissolution within each cell can be related, cell by cell, to the flux of reactant J_0 entering the system. Pore scale simulations reported in Section 3 show that the coefficients α_n are universal functions of the local porosity $\alpha_n = \alpha(\varphi_n)$ (Section 3.5). Results for periodic arrays of thin cylinders (disks) were used to construct a one-dimensional flux-based upscaling scheme. With constitutive models for the mass transfer coefficients determined from a small number of unit cells, the evolution of porosity of a much larger system can be determined from solutions of an ordinary differential equation for each REV (Section 3.6).

2. Simulation model and methods

Pore structures were created from periodic arrays of thin cylinders as indicated in Fig. 1. Square arrays (Fig. 1a) contained 20 unit cells (only 10 are shown), while the hexagonal arrays (Fig. 1b) contains 10 unit cells with two cylinders per unit cell. The pore structures were based on recent simulations and experiments with a single gypsum disk, radius $R = 10$mm and thickness $d = 0.5$mm, confined within a Hele-Shaw cell with a gap of 0.5mm between the plates (Dutka et al., 2020; Ladd et al., 2020). Numerical simulations showed that dissolution within a narrow Hele-Shaw cell is essentially two-dimensional; diffusion rapidly smears out variations in concentration over the small height of the disk (0.5mm).

For the size of disk used in the experiments, dissolution was largely limited by the diffusion of ions away from the disk. A comparison of the shapes and sizes of the dissolving disk served as a validation of the pore-scale physics on a local as well as a global scale, meaning that the distribution of fluxes around the disk, as well as the overall dissolution rate, were in quantitative agreement with experiment (Dutka et al., 2020). In this work we maintain the focus on transport-limited dissolution, but investigate more realistic pore structures comprising periodic arrays of disks with a narrow gap ($0.05R - 0.075R$) between the grains.

Fluid motion in a Hele-Shaw cell can be approximated as a lubrication flow, with a vertically-averaged velocity between the plates $\overline{\boldsymbol{u}} = d^{-1}\int_0^d \boldsymbol{u}\,\mathrm{d}z$. The force balance includes the drag exerted by the boundaries of the Hele-Shaw cell $\xi\overline{\boldsymbol{u}}$, where $\xi = 12\mu/d^2$ and μ is the fluid viscosity. The Reynolds number under the condition of the experiments (Dutka et al., 2020) is small ($Re = u_0 d/\nu < 0.01$), and inertial terms in the force balance can be neglected:

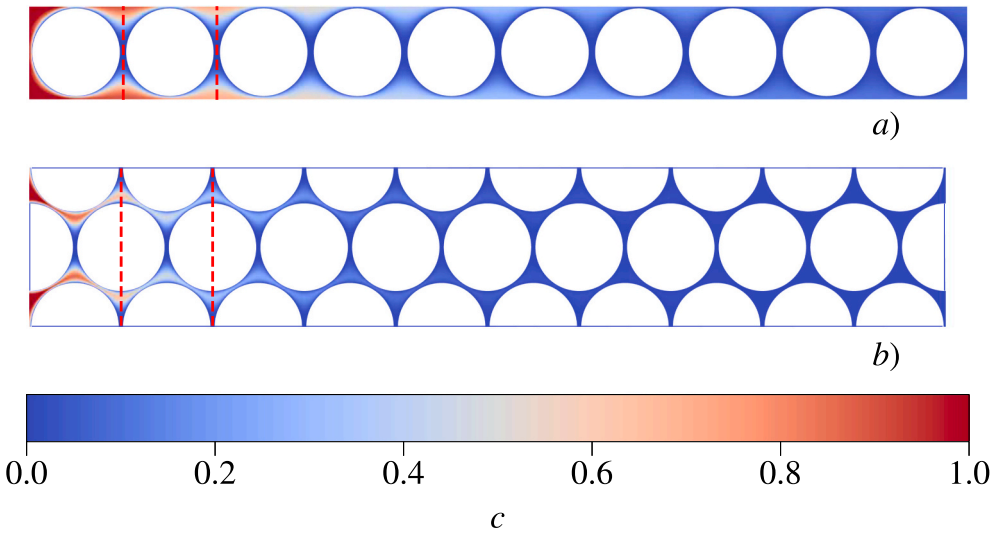

Fig. 1. Illustrations of the pore structures used in this work; the vertical boundaries are periodic, creating a matrix of infinite vertical extent. The velocity field in each unit cell is the same, with a mean value of u_0. (a) Square array of unit cells ($l_x = 2.15R \times l_y = 2.15R$) with a porosity of 32%; only the first 10 of the 20 cells in the system are shown. (b) Hexagonal array with 2 disks per unit cell ($l_x = 2.1R \times l_y = 3.64R$); the porosity is 18%. The vertical red lines show the boundaries of a single unit cell. The color field indicates the steady-state concentration field at Pe = 100. (For interpretation of the references to color in this figure legend, the reader is referred to the web version of this article.)

$$\nabla p = \mu \nabla^2 \overline{\boldsymbol{u}} - \xi \overline{\boldsymbol{u}}, \tag{1}$$

where the pressure p is determined by the incompressibility condition,

$$\nabla \cdot \overline{\boldsymbol{u}} = 0. \tag{2}$$

We assume no slip conditions on the pore surfaces and a uniform velocity $\overline{u}_x = u_0$ at the inlet.

Transport of reactants follows a convection-diffusion equation

$$\nabla \cdot (\overline{\boldsymbol{u}}\, \overline{c}) = D \nabla^2 \overline{c}, \tag{3}$$

where D is the molecular diffusion coefficient, and $\overline{c}(x,y) = (d|\overline{\boldsymbol{u}}|)^{-1} \int_0^d (\boldsymbol{u}c) \mathrm{d}z$ is the velocity-averaged concentration field (Bird et al., 2001). However, in this geometry $c(x, y, z)$ is essentially independent of z, so here the distinction is not very important. In order to emphasize the effects of reactant transport, we assume the surface reaction is fast enough that the solution at the pore surface is in equilibrium. A Dirichlet boundary condition

$$\overline{c} = 0 \tag{4}$$

is used on all the pore surfaces. Reactant enters the system (from the left in Fig. 1) with a flux $u_0 c_{\mathrm{in}}$. A Danckwerts boundary condition was imposed at the inlet

$$\left(\overline{u}_x \overline{c} - D \frac{\mathrm{d}\overline{c}}{dx} \right)_{x=0} = u_0 c_{\mathrm{in}}, \tag{5}$$

which approximates the condition when there is an inert region upstream of the soluble material. Since the reaction rate constant is essentially infinite (4), there is a single parameter governing the transport equations, namely the Péclet number

$$\mathrm{Pe} = \frac{u_0 R}{D}. \tag{6}$$

At sufficiently high Pe, Eq. (5) reduces to a Dirichlet condition $c(x = 0) = c_{\mathrm{in}}$.

With the assumption that the surface reactions are instantaneous, the dissolution rate is controlled by diffusion of ions near the pore surfaces. The diffusive flux at the pore-fluid interface controls the (normal) motion of the surface points as the solid matrix dissolves,

$$c_{\mathrm{sol}} \frac{\mathrm{d}\boldsymbol{x}}{\mathrm{d}t} = -D \boldsymbol{n} (\boldsymbol{n} \cdot \nabla \overline{c})|_S, \tag{7}$$

where c_{sol} is the concentration of ions in the mineral phase. The characteristic time scale for the evolution of the pore space $\tau = R/(u_0 \gamma)$, where $\gamma = c_{\mathrm{in}}/c_{\mathrm{sol}}$ is the ratio of molar concentrations in the aqueous and mineral phases. Since interface motion is extremely slow in comparison with the time scales for reactant transport (Starchenko et al., 2016), the stationary limit of the convection-diffusion Eq. (3) is sufficient.

Eqs. (1)–(7) were solved using a finite-volume discretization, implemented with the OpenFOAM toolkit (Starchenko et al., 2016; Starchenko and Ladd, 2018). Results are reported in terms of dimensionless quantities, using the radius of the disk R, the inlet velocity u_0, and the reactant concentration c_{in} as the natural scales:

$$\boldsymbol{x} \to \frac{\boldsymbol{x}}{R} \qquad \boldsymbol{u} = \frac{\overline{\boldsymbol{u}}}{u_0} \qquad t \to \frac{t}{\tau} = \frac{u_0 \gamma t}{R} \qquad c = \frac{\overline{c}}{c_{\mathrm{in}}}. \tag{8}$$

Further details of the numerical methods and validations for the Hele-Shaw geometry can be found in Dutka et al. (2020) and Ladd et al. (2020).

3. Results

Classical upscaling methods (Brenner, 1980; Whitaker, 1986; Auriault and Adler, 1995; Battiato and Tartakovsky, 2011) invoke a separation between macroscopic and pore-scale variations in the fields. For the concentration field this is usually expressed as a power series in the ratio of pore size l to the sample dimension L, $\varepsilon = l/L$ (Auriault and Adler, 1995; Battiato and Tartakovsky, 2011):

$$c(\boldsymbol{X}, \boldsymbol{x}) = c_0(\boldsymbol{X}) + \varepsilon (\nabla_x c_0(\boldsymbol{X}) \chi(\boldsymbol{x}) + c_1(\boldsymbol{X})), \tag{9}$$

where $\chi(\boldsymbol{x})$ is a periodic function describing the variation of concentration within an REV. The field c_0 is a solution of the convection diffusion-equation with non-reactive (zero-flux) boundary conditions. In a multiscale expansion $\boldsymbol{X}$ describes variations on the macroscopic scale, while $\boldsymbol{x}$ is a pore-scale coordinate. Alternatively, the fields c_0 and c_1 can be found from averages over a unit cell (Brenner, 1980; Whitaker, 1986; Golfier et al., 2002).

However, classical upscaling is limited to cases where the reaction rate is small, or when $kL/D \ll 1$ (Battiato and Tartakovsky, 2011). In the present case, the reaction rate is limited by diffusion across the boundary layer around the disk, so that $k_{\mathrm{eff}} = D/\delta$, where δ is the boundary layer thickness. Since δ is less than the pore size, the upscaling conditions cannot be satisfied. Here we make a preliminary exploration of a different approach, focusing on tracking the concentration flux entering and leaving a given REV. We begin with the undissolved pore structure (Sections 3.1 and 3.2), where each unit cell has an identical pore space. The remainder of the results (3.3–3.6) include dissolution of the solid matrix.

3.1. Pore-scale concentration fields

Results from pore-scale simulations of square and hexagonal arrays of disks are shown in Fig. 1 at a Péclet number Pe = 100 (6). The velocity field is periodic, but the concentration field decays rapidly along the flow (x) direction, with a penetration length $l_p \approx 3l_x$, where $c(l_p) = e^{-1}$. A more detailed view of the concentration field in three successive disks is shown in the left panels of Fig. 2 at Péclet numbers of 1, 10, 100. The cells shown in the figure were selected so that the central cell is beyond the penetration length, l_p, which can be inferred from the decay of the inlet flux to each unit cell, shown in Fig. 3.

Figs. 1 and 2 show that there is no clear separation of scales, even at the highest Péclet number. The concentration field decays over length scales comparable to the pore size, and the scale separation implicit in Eq. (9) does not apply in this case. Nevertheless, it is still possible to exploit the periodic nature of the pore space by making the macroscopic coordinate discrete rather than continuous, $X_n = nl_x$. Cell n ($n = 1, 2, 3, \ldots$) is bounded by the inlet plane X_{n-1} and outlet plane X_n and a location within the cell has the absolute coordinate $X_{n-1} + x$. A surprising result from pore-scale simulations (Fig. 2) is that the spatial variations of concentration within each unit cell are very similar. In fact, concentration fields in successive cells exhibit a multiplicative scaling based on the inlet flux to each cell:

$$c_n(\boldsymbol{x}) = j_{n-1} \chi(\boldsymbol{x}), \tag{10}$$

where $j_{n-1} = l_y^{-1} \int_0^{l_y} j_x(X_{n-1}, y)\, \mathrm{d}y$ is the average concentration flux crossing the inlet to cell n. Since the spatial variation of concentration within each unit cell is the same, $\chi(\boldsymbol{x})$ is independent of n, although it is not periodic in the flow direction, as in Eq. (9). Note that the macroscopic coordinate is undefined inside the cells; it only exists on the inlet/outlet faces.

The form of the concentration field (10) is validated by the data in

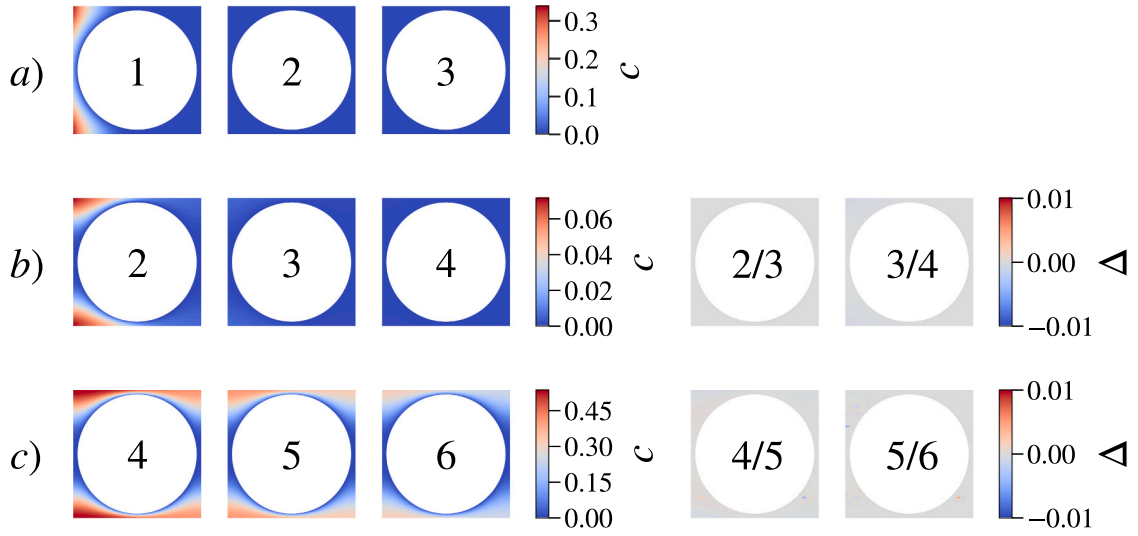

Fig. 2. Concentration fields in different unit cells (left panel), and ratios of concentrations in successive pairs of cells (right panel). Results are shown for different Péclet numbers: (a) Pe = 1, (b) Pe = 10, and (c) Pe = 100. The right panels show the extent to which the concentration field deviates from the scaled periodic function suggested by Eq. (10). The images are maps of the concentration ratios $\Delta_n = (c_n/j_{n-1})/(c_{n+1}/j_n) - 1$ for two successive cells n and $n+1$. At Pe = 1, the flux of concentration into the second cell is negligible and no mapping is possible.

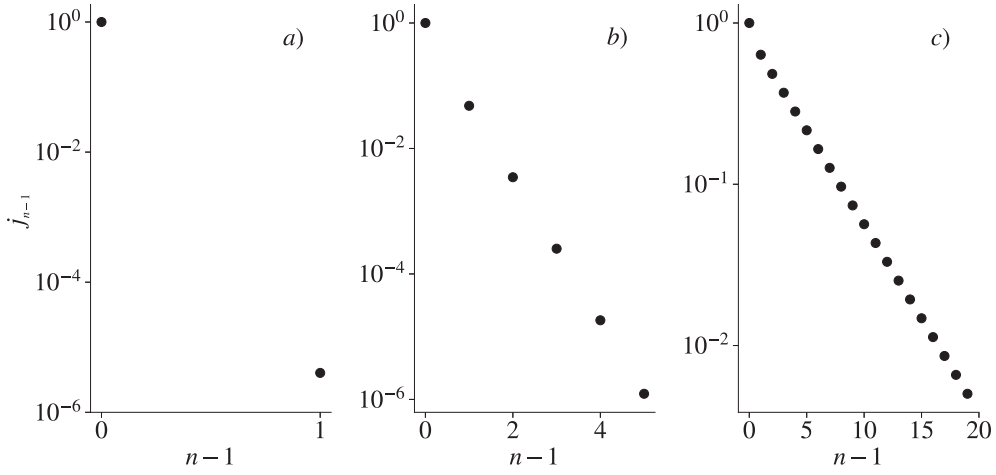

Fig. 3. Inlet fluxes to cell n, $j_{n-1} = J_{n-1}/l_y$ at different Péclet numbers: (a) Pe = 1, (b) Pe = 10, (c) Pe = 100. The penetration length l_p corresponds to a decay in the flux by a factor e.

Fig. 2. At low Péclet numbers (Pe = 1) the inlet flux is entirely absorbed within the first cell (Fig. 2a). The flux at the inlet to cell 2 (j_1) is roughly 6 orders of magnitude smaller than j_0 (Fig. 3); this simply means that $c_n(\boldsymbol{x}) = 0$ for $n > 1$. At higher Péclet numbers, unconsumed reactant penetrates into successive cells, but the distribution of c is the same except for cells closest to the inlet X_0. The right panel shows ratios of concentrations in successive cells $\Delta_n = (c_n/j_{n-1})/(c_{n+1}/j_n) - 1$. A uniform value $\Delta_n = 0$ implies that Eq. (10) holds for both those cells. At Pe = 10, $\Delta_1 = \chi_1/\chi_2 - 1$ deviates from zero around the leading edge of the disk, but the ratios Δ_2 and Δ_3 are spatially uniform to better than 1%. Similar results hold for pairs of disks deeper inside the matrix. At Pe = 100 the concentration fields away from the inlet region (by $n = 4$) also follow Eq. (10) precisely. Importantly, the mutliplicative scaling leading to the uniform maps of Δ_n are not arbitrary, but are connected to the average fluxes j_n crossing the planes between cells n and $n+1$. These fluxes are shown in Fig. 3.

3.2. Pore-scale fluxes

Upscaling the concentration field is uncertain in general, requiring assessments of the reactive surface area within the REV, as well as values for the surface dissolution rate constant. When transport effects are significant, it is not even clear how to define the bulk (or pore-scale averaged) concentration in a way that can be connected to surface dissolution rates. In the end, all the uncertainties are usually swept up into an effective reaction rate (or mass-transfer coefficient), which serves as both a source term in the macroscopic concentration equation and as a basis to compute the dissolution rate of the mineral. However, instead of formulating a macroscopic equation for the concentration, here we simply keep track of the fluxes crossing each face of the REV. We consider a periodic porous medium, as in Fig. 1, with flow in the x direction. At the inlet surface (left end), the flux is determined from a Danckwerts boundary condition, which in dimensionless form is:

$$j_0 = (u_x c - D\partial_x c)_{X=0} = 1. \tag{11}$$

This imposes a constant flux at the inlet, which is convenient for subsequent calculations. At high Péclet numbers it is equivalent to a constant inlet concentration $c(X = 0) = 1$.

For the geometries shown in Fig. 1 the flow in each unit cell is the same, and according to Eq. (10) the concentration in each cell differs only in its overall magnitude. The total mass flux absorbed by disk n is the integral of the diffusive current $\boldsymbol{n} \cdot \nabla c$ over the surface of the disk $J_n^{\text{abs}} = \int_{S_n} (\boldsymbol{n} \cdot \nabla c) d\boldsymbol{x}$. Applying the ansatz for the concentration field from Eq. (10) gives an expression for absorbed flux as a fraction of the inlet flux, $J_{n-1} = j_{n-1} l_y$:

$$J_n^{\text{abs}} = \frac{J_{n-1}}{l_y} \int_{S_n} (\boldsymbol{n} \cdot \nabla \chi(\boldsymbol{x})) d\boldsymbol{x} = \alpha J_{n-1}. \tag{12}$$

The uniformity of χ shown in Fig. 2 implies that α is independent of n (at $t = 0$).

The unabsorbed reactant is passed to the next cell, $J_n = (1 - \alpha) J_{n-1}$, which results in an exponential decay of the total flux entering successive cells. Fig. 3 shows the inlet mass flux for three different Péclet numbers: Pe = 1, 10, 100. At Pe = 100, the decay is perfectly exponential, except for the cell nearest the inlet. It is not surprising that an average property such as α is less sensitive to the cell position than the concentration field itself, where the inlet effects persisted 4 or 5 unit cells into the matrix (Fig. 2). At Pe = 10 the decay is exponential from the beginning, consistent with the smaller penetration length. Finally, at the lowest Péclet numbers (Pe = 1), the reactant is almost totally absorbed within the first unit cell (at $t = 0$), and the outlet flux j_1 can scarcely be detected over the numerical uncertainties

3.3. Dissolution

As the solid matrix dissolves, grains in different unit cells evolve with a variety of shapes and sizes; examples are shown in Fig. 4. At high Péclet numbers, single grains take up a lemniscate shape as they dissolve (Soulaine et al., 2017; Dutka et al., 2020; Ladd et al., 2020), with the pointed end in the downstream direction. A similar shape is observed in a high porosity array of disks, shown in Fig. 4a. Soulaine et al. (2017) reports similar shapes at high Péclet and Damköhler numbers, as shown in their Figure 9. Interestingly, dissolution of grains appears to be a stable process, where small perturbations to the grain shape tend so smooth out over time. Observations of the dissolution of individual gypsum grains over periods of about 30 days showed small but significant asymmetries in the grain shape (Dutka et al., 2020), due to varying conditions that were difficult to control over such long periods of time. Nevertheless, these variations in shape tended to diminish as the grain dissolved further, suggesting that particular shapes are especially stable, or "attractors" in the language of non-linear dynamical systems. Numerical simulations also suggest that the shapes of dissolving disks are robust to variations in the numerical method (Molins et al., 2020).

At porosities more closely related to real rocks, the additional confinement produces more symmetric shapes. For a square array ($\varphi(0) = 0.32$) the disks become oval in shape, while in hexagonal arrays ($\varphi(0) = 0.177$) they take on a diamond shape. In both cases there is a remarkable degree of for-aft symmetry, which is quite unlike the higher porosity cases (Soulaine et al., 2017; Ladd et al., 2020). At lower Péclet numbers the symmetry is broken, but in this case the pointed tip is directed upstream. The asymmetry persists down to Pe = 1, whereas for more dilute arrays (or single disks) the shape remains circular (Soulaine et al., 2017; Ladd et al., 2020). Thus, the high degree of confinement leads to significantly different shapes from an isolated disk or a dilute array.

Although the shapes of disks in different cells are not the same (Fig. 4), it turns out that each disk passes through an almost identical sequence of shapes, regardless of its position in the matrix. Thus for any pair of disks, not too close to the inlet, the shape $S_n(t)$ is exactly the same as the shape of a different disk at a related time $S_{n'}(t')$. Examples of these shape mappings are shown in Fig. 5. Each panel shows the disks closest to the inlet that have an exact mapping of their shapes. Disks deeper into the porous matrix have similar mappings, which hold across different Péclet numbers and initial pore structures. The mapping for the high porosity unit cell (Fig. 4a) is similarly precise.

If the disk shapes in two different cells are the same, then it follows

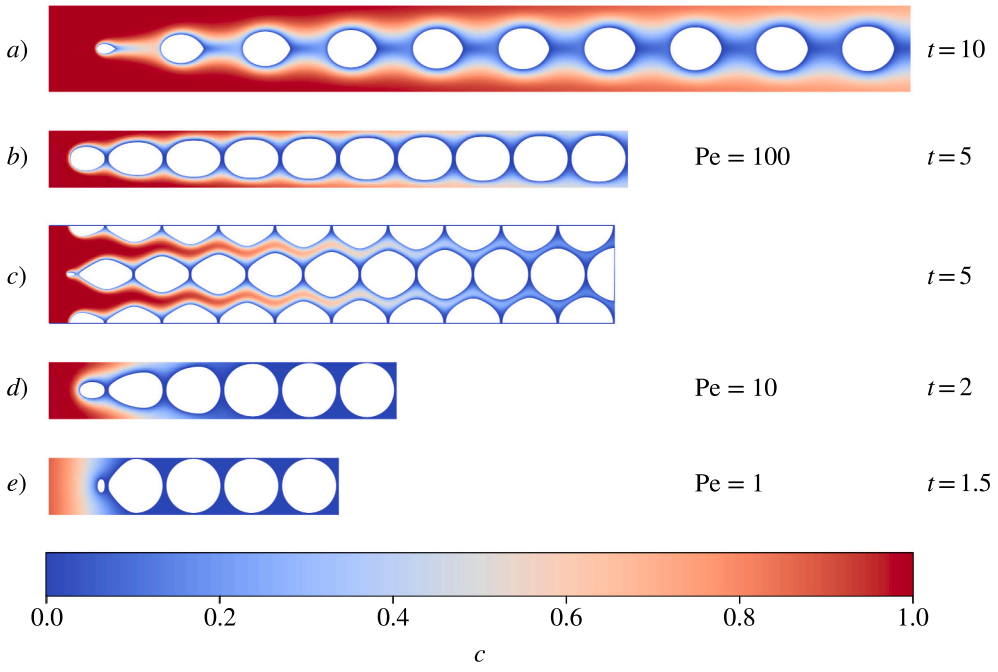

Fig. 4. Evolution of concentration field and disk shape for different initial geometries and Peclet numbers: (a) square array, $\varphi_0 = 0.693$, Pe = 100; (b) square array, $\varphi_0 = 0.320$, Pe = 100; (c) hexagonal array, $\varphi_0 = 0.177$, Pe = 100; and (d) square array, $\varphi_0 = 0.320$, Pe = 10; (e) square array, $\varphi_0 = 0.320$, Pe = 1.

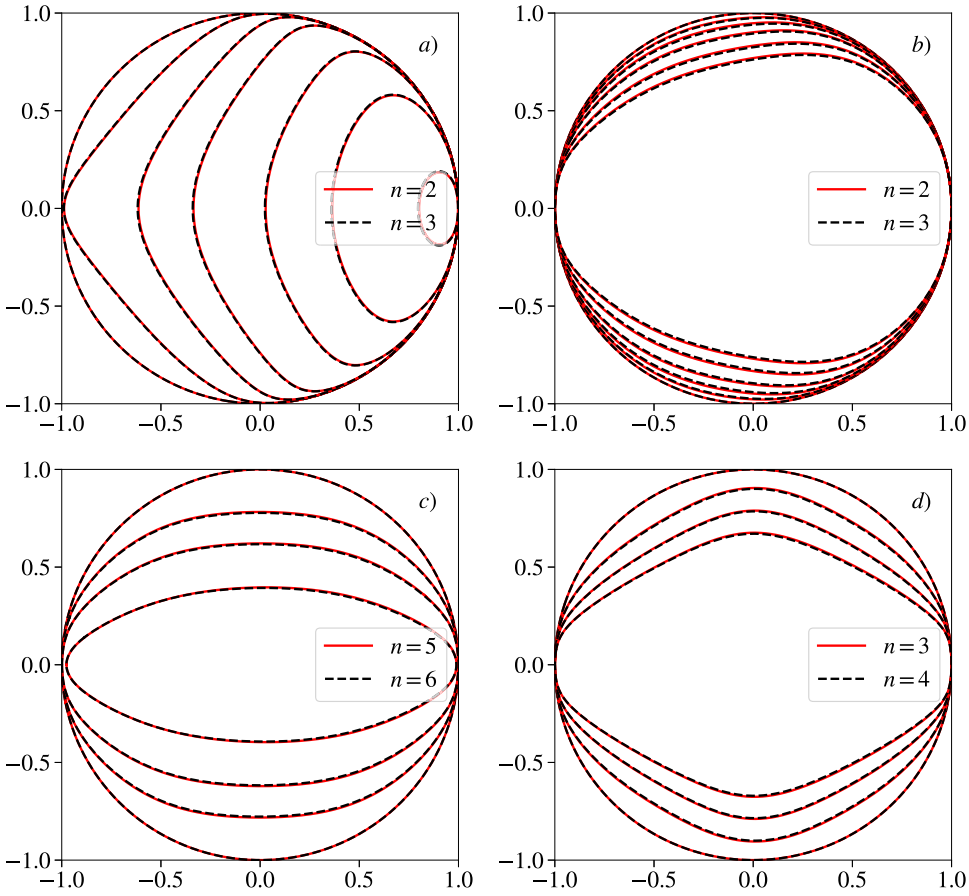

Fig. 5. Shapes of successive disks at two different times t_n and $t_{n+1}(t_n)$. Results are shown for different Peclet numbers and initial pore structures: (a) square array, Pe = 1; (b) square array, Pe = 10; (c) square array, Pe = 100; (d) hexagonal array, Pe = 100. In panel (d) the index refers to the disk centered on face n (starting at $n = 0$).

that the porosity in those cells is also the same. This suggests that the evolution of the pore structure (grain shapes) can be characterized by the time-dependent porosity combined with the initial pore structure and Péclet number:

$$S_n(t) = S(\varphi_n(t), S, \mathrm{Pe}). \tag{13}$$

The evolution of disk shapes shown in Fig. 4 are all described by Eq. (13), which applies to all the cells that are not adjacent to the inlet.

3.4. Permeability evolution

The velocity field in a periodic pore space $\boldsymbol{u}_n(\boldsymbol{x}, t = 0)$ is the same in every unit cell. Here we investigate if the scaling from Eq. (13) can be applied to determine the flow field in systems where the initial periodicity is broken by dissolution (see Fig. 4). We try the following ansatz for the velocity field, suggested by Eqs. (10) and (13),

$$\boldsymbol{u}_n(\boldsymbol{x}, t) = q_{n-1}\boldsymbol{\psi}(\boldsymbol{x}, \varphi_n(t), S, \mathrm{Pe}), \tag{14}$$

where $\boldsymbol{\psi}$ is independent of the cell index, and $q_{n-1} = l_y^{-1}\int_0^{l_y} u_x(X_{n-1}, y)\,\mathrm{d}y$ is the average fluid flux entering cell n. This is consistent with classical upscaling theories, which assume that the permeability is a local function of the porosity. However, the remaining parameters (S, Pe) are not empirical functions such as tortuosity (for example), but characterize the pore-scale properties of specific initial conditions. For the pore structures shown in Fig. 4 q_n is constant, but in more general geometries fluid would flow from more than one direction. In such cases the velocity field ($\boldsymbol{u}_n$) would be a sum of contributions from each inlet face, with varying inlet and outlet fluxes.

The permeability of a unit cell can be calculated from the integrated pressure over the inlet and outlet faces, $P_n = \int_0^{l_y} p(X_n, y)\,\mathrm{d}y$, as $K_n^{-1} = (P_{n-1} - P_n)/(\mu q_{n-1} l_x l_y)$. This suggests a universal relation for the permeability by analogy with (13),

$$K_n(t) = K(\varphi_n(t), S, \mathrm{Pe}). \tag{15}$$

However, after dissolution, Eq. (14) is no longer exact. The mapping (13) is local to each cell, while the flow in each cell is affected by the different grain shapes in the upstream and downstream cells. However, if the grain sizes are not too dissimilar, it might be expected that Eq. (14) is a reasonable approximation to the flow in each unit cell. The hypothesis is supported by the data in Fig. 6, which shows that the permeability at the same φ, S, Pe is the same in all unit cells, except for the first cell in the array.

3.5. Mass transfer during dissolution

Mass transfer at the pore surfaces can be expressed in terms of the absorbed fraction (α_n) of the flux (J_{n-1}) entering cell n. The reactive flux, integrated over the pore surface in cell n is $J_n^{\mathrm{abs}} = \alpha_n(t)J_{n-1}(t)$ (12). As the matrix dissolves, $\alpha_n(t)$ is no longer independent of n, but if the mapping from Eq. (13) holds for mass transfer as well as for permeability then we would expect a universal equation for α_n,

$$\alpha_n(t) = \alpha(\varphi_n(t), S, \mathrm{Pe}), \tag{16}$$

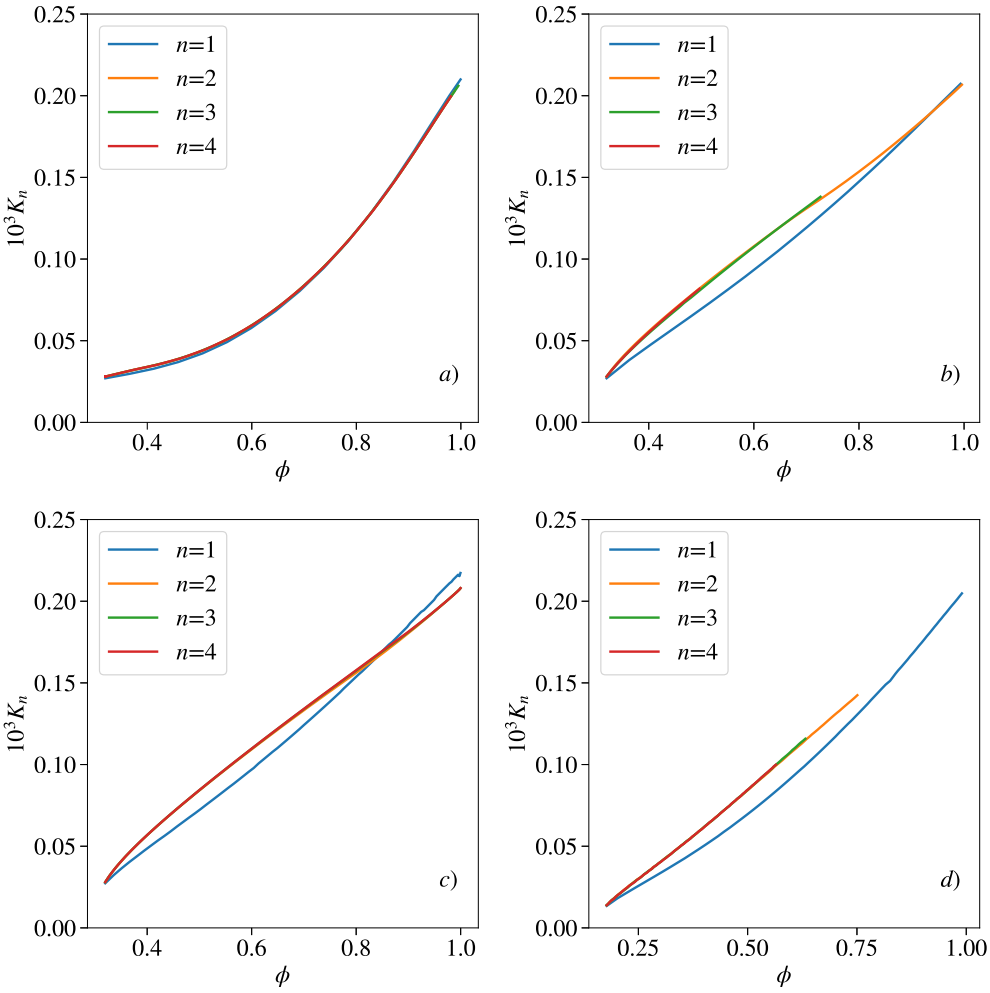

Fig. 6. Permeability $K_n(\varphi)$ of individual unit cells. Results are shown for different Peclet numbers and pore structures: (a) square array, Pe = 1; (b) square array, Pe = 10; (c) square array, Pe = 100; (d) hexagonal array, Pe = 100.

independent of n. Results for α_n from pore scale simulations are shown in Fig. 7. In general, disks away from the inlet have similar mass transfer coefficients at each porosity. The first disk tends to be anomalous because it has no disk ahead of it to shield it from the reactant.

Fig. 7a shows mass transfer coefficients in a square array at a low Péclet number (Pe = 1). In this case one cell is almost completely dissolved ($\varphi \approx 1$) before the next cell starts dissolving (see Fig. 4e). Thus every disk behaves more or less as the first disk in the array. The mass transfer coefficient is close to unity (meaning almost no reactant escapes the first unit cell) until the porosity reaches approximately 75%. At this point α decreases rapidly to zero as the disk vanishes. A logarithmic singularity at low Péclet numbers was also found in the dissolution of individual disks (Rycroft and Bazant, 2016; Ladd et al., 2020).

At Pe = 10 (Fig. 7b), there are two distinct curves for α_n; one for the first disk and another for the remaining disks in the array. The interior disks have very similar values of α_n, until at a critical porosity they switch from the generic functional form for α to the one characteristic of the first disk. The pore-scale data shows that this corresponds to the point in time where the upstream disk has just fully dissolved. For example, when the porosity in cell 2 reaches about 70%, the disk in cell 1 has just dissolved entirely. This removes the shielding of the concentration field by the upstream disk, which persists down to very small areas as can be seen (for example) in Fig. 4c. The final stages of dissolution ($\varphi > 0.8$) are universal, and similar to the dissolution of an isolated disk (Ladd et al., 2020).

At higher Péclet numbers (Pe = 100), the increased penetration length of the reactant means that mass transfer in the first two or three disks is higher than in the subsequent disks in the array (Fig. 7c). The jump in reaction rate when the lead disk is fully dissolved propagates into the array, leading to smaller but still noticeable jumps in dissolution rate in the interior. The increased penetration length at high Pe makes the locality assumption (13) less accurate than at lower flow rates. However the effect of the entry region on the overall dissolution is small (see Section 3.6). Finally, the mapping of the mass transfer coefficient remains valid for different pore architectures. Fig. 7d shows the same behavior for the hexagonal array as for the square array.

3.6. An REV scale model for dissolution

We can assemble the insights from these pore-scale simulations into an REV scale model for dissolution. Since the flow in these systems is one dimensional, the average fluid flux across each inlet face is the same ($q_n = q_0$). Therefore, we consider only the mass transfer, which can be formulated in terms of the evolution of the porosity within each unit cell. Noting that the acid capacity, γ, has been absorbed into the time scale (Eq. (8)), the evolution of porosity at the REV scale is described by:

$$\frac{\mathrm{d}\varphi_n}{\mathrm{d}t} = \alpha_n(t) J_n(t). \tag{17}$$

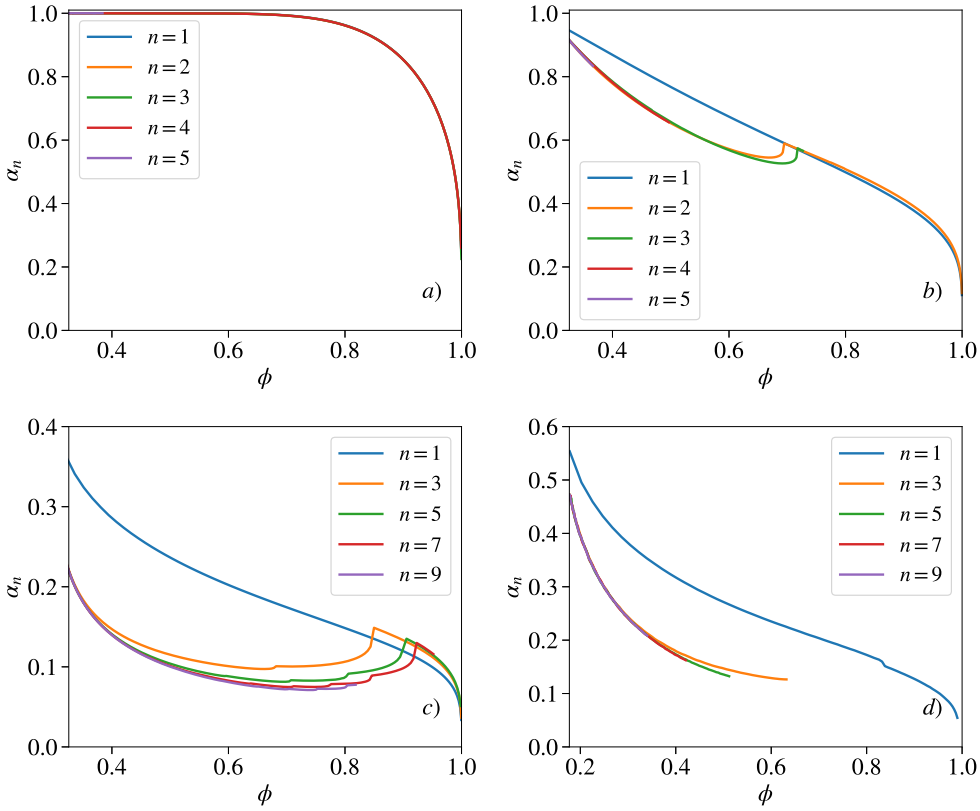

Fig. 7. Mass transfer coefficients $\alpha_n(\varphi)$ versus porosity; α_n is the fraction of the inlet flux to cell n that is absorbed by dissolution within the cell, and φ_n is the porosity of unit cell n. Results are shown for different Peclet numbers and initial geometry: (a) square array, Pe = 1; (b) square array, Pe = 10; (c) square array, Pe = 100; (d) hexagonal array, Pe = 100.

The inlet fluxes are calculated from the recursion relation $J_n = (1 - \alpha_n)J_{n-1}$, with $J_0 = l_y$, while α_n is found from pore-scale data using the ansatz (16). For the comparison shown in Fig. 8, we used two values of $\alpha(\varphi_n)$: one for the lead disk in the array (α_0) and one for all the interior disks. It can be seen the two-α model is sufficient to capture the evolution of porosity (and mass transfer) in all cases. The comparisons in Fig. 8 show that the model captures the time-dependent porosity much deeper into the matrix than the disks used to parametrize $\alpha(\varphi)$, which are indicated in the figure caption. The model simulations can be easily extended to much longer times and much larger domains, because simulations at the REV scale take orders of magnitude less computing than simulations at the pore-scale.

4. Discussion

In this paper we have investigated the dissolution of simple periodic pore structures, with a view to understanding how such simulations can be upscaled in cases where the reaction rate is high and the dissolution is limited by ion transport. The work is complementary to previous investigations (Golfier et al., 2002) where pore-scale data can only be upscaled at low reaction rates (Battiato and Tartakovsky, 2011). Fig. 8 in Guo et al. (2021) illustrates the breakdown in classical upscaling when the Damköhler number is large. By contrast, in Fig. 1 we find near perfect agreement between pore-scale and upscaled models, even though the Damköhler number is essentially infinite.

In this work we have taken a first step towards an upscaling method for large Damköhler numbers. The model does not require equations for the velocity and concentration fields, but directly calculates fluxes entering and leaving each unit cell within a discrete array of REV's. The constitutive models for mass transfer $\alpha(\varphi, S, \mathrm{Pe})$ and momentum transfer $K(\varphi, S, \mathrm{Pe})$ are calculated from the dissolution of a small number of unit cells. The key approximation, that the local permeability and mass transfer coefficients can be replaced by functions of porosity and initial conditions, has been partially validated by comparisons with pore-scale simulations of unidirectional flows. It would be of significant interest if these ideas could be extended to more general geometries and flows.

A number of interesting features emerged from the pore-scale simulations. In the initial periodic array there is an exact mapping of the velocity field from one unit cell to another. More surprisingly, this holds for the concentration field as well when scaled by a single factor, the total flux of concentration entering the cell. As the porous matrix dissolves, grains in different unit cells pass through exactly the same sequence of shapes, although at different rates. This observation is a validation of the common assumption that the constitutive properties of the porous matrix are functions of the local porosity. However, the variable set must be augmented by the initial pore structure and Péclet number. If surface reactions are sufficiently slow, the Damköhler number would also be a parameter.

We could identify three different regimes of dissolution: free, shielded, and porous. The leading disk in the array is attacked by a more or less unperturbed reactant field, and dissolves in a similar way to a single disk (Ladd et al., 2020). These are the blue lines in Fig. 7, which we call "free dissolution". When the area of the leading disk is small but non-zero, the disks immediately behind it are shielded to a significant extent, even though the area of the shielding disk is small. This effect can be seen in the concentration fields in Figs. 4a and 4c; the shielded disk has a lower dissolution rate, than when the leading disk vanishes entirely. This leads to the upturn in $\alpha(\varphi)$ illustrated in Figs. 7b and 7c. Once the leading disk dissolves, the shielded disk switches to the free dissolution regime. Further into the porous matrix, dissolution is essentially universal and

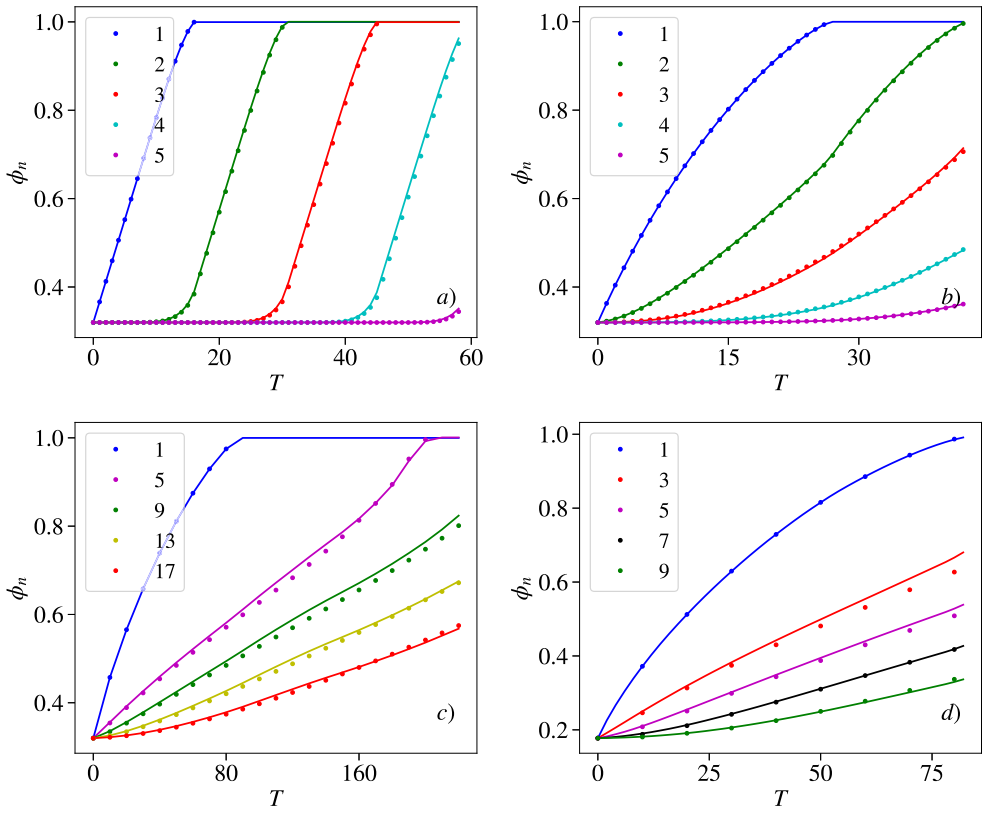

Fig. 8. Evolution of porosity with time in different unit cells, as indicated in the legend. The solid lines are the results of numerical simulation and the dots are the results of the REV scale model. Results are shown for different Peclet numbers and initial geometry: (a) square array, Pe = 1; (b) square array, Pe = 10; (c) square array, Pe = 100; (d) hexagonal array, Pe = 100. The unit cells used to create the two α values were: (a) 1, 1; (b) 1, 2; (c) 1, 5; (d) 1, 2.

$\alpha(\varphi)$ is independent of the cell index. Combining these ideas allows for a simple model for the dissolution of the matrix, which is in quantitative agreement with the pore-scale simulations (Fig. 8). The shielded regime is not universal but it is of short duration, and does not significantly affect the evolution of porosity. Thus Fig. 8 was constructed with just two values of α: one corresponding to free dissolution and the other to the universal porous regime.

In this work we used a two-dimensional computational domain to allow for more rapid calculations, but three-dimensional simulations are feasible as well. The key connections would remain: the scaling of concentration between cells and the mapping of shapes between different unit cells. However, we have not addressed what happens in more complex flows, where the fluid flux crosses more than two faces of the REV. In the high velocity limit, the concentration flux across each face would be proportional to the fluid flux, but there will be diffusive contributions as well at smaller Péclet numbers (on the REV scale). Formulating an upscaling for complex REV's where there is significant fluid flow transverse to the main axis remains a challenge.

Declaration of Competing Interest

The authors declare that they have no known competing financial interests or personal relationships that could have appeared to influence the work reported in this paper.

Acknowledgements

This work was supported by the U.S. Department of Energy, Office of Science, Office of Basic Energy Sciences, Chemical Sciences, Geosciences, and Biosciences Division under Award Number DE-SC0018676, and by the National Science Center (Poland) under research Grant No. 2016/21/B/ST3/01373.

References

Auriault, J., Adler, P., 1995. Taylor dispersion in porous media: analysis by multiple scale expansions. Adv. Water Res. 18, 217–226. https://doi.org/10.1016/0309-1708(95)00011-7.

Battiato, I., Tartakovsky, D.M., 2011. Applicability regimes for macroscopic models of reactive transport in porous media. J. Contam. Hydrol. 120-21, 18–26. https://doi.org/10.1016/j.jconhyd.2010.05.005.

Beinlich, A., Plümper, O., Hövelmann, J., Austrheim, H., Jamtveit, B., 2012. Massive serpentinite carbonation at Linnajavri. N-Norway. Terra Nova 24, 446–455. https://doi.org/10.1111/j.1365-3121.2012.01083.x.

Bird, R.B., Stewart, W.E., Lightfoot, E.N., 2001. Transport Phenomena. John Wiley & Sons, Department of Chemical Engineering. Madison, Wisconsin.

Brenner, H., 1980. Dispersion resulting from flow through spatially periodic porous media. Philos. Trans. Royal Soc. A. 297, 81–133. https://doi.org/10.1098/rsta.1980.0205.

Dutka, F., Starchenko, V., Osselin, F., Magni, S., Szymczak, P., Ladd, A.J., 2020. Time-dependent shapes of a dissolving mineral grain: comparisons of simulations with microfluidic experiments. Chem. Geol. 540, 119459. https://doi.org/10.1016/j.chemgeo.2019.119459.

Elkhoury, J.E., Ameli, P., Detwiler, R.L., 2013. Dissolution and deformation in fractured carbonates caused by flow of CO_2-rich brine under reservoir conditions. Int. J. Greenhouse Gas Control 16, S203–S215. https://doi.org/10.1016/j.ijggc.2013.02.023.

García-Ríos, M., Luquot, L., Soler, J.M., Cama, J., 2015. Influence of the flow rate on dissolution and precipitation features during percolation of CO_2-rich sulfate solutions through fractured limestone samples. Chem. Geol. 414, 95–108. https://doi.org/10.1016/j.chemgeo.2015.09.005.

Golfier, F., Bazin, B., Lenormand, R., Quintard, M., 2004. Core-scale description of porous media dissolution during acid injection - Part I: Theoretical development. Comput. Appl. Math. 23, 21. https://doi.org/10.1590/S0101-82052004000200005.

Golfier, F., Quintard, M., Bazin, B., Lenormand, R., 2006. Core-scale description of porous media dissolution during acid injection - Part II: Calculation of the effective properties. Comput. Appl. Math. 25, 23. https://doi.org/10.1590/s1807-03022006000100003.

Golfier, F., Quintard, M., Whitaker, S., 2002. Heat and mas transfer in tubes: an analysis using the method of volume averaging. J. Porous Med. 5, 169–185. https://doi.org/10.1615/jpormedia.v5.i3.10.

Guo, J., Laouafa, F., Quintard, M., 2021. Large-scale model for the dissolution of heterogeneous porous formations: theory and numerical validation. Trans. Porous Med. https://doi.org/10.1007/s11242-021-01623-0.

Guo, J., Veran-Tissoires, S., Quintard, M., 2016. Effective surface and boundary conditions for heterogeneous surfaces with mixed boundary conditions. J. Comp. Phys. 305, 942–963. https://doi.org/10.1016/j.jcp.2015.10.050.

Koeshidayatullah, A., Corlett, H., Hollis, C., 2021. An overview of structurally-controlled dolostone-limestone transitions in the stratigraphic record. Earth Sci. Rev. 220, 103751. https://doi.org/10.1016/j.earscirev.2021.103751.

Ladd, A.J.C., Szymczak, P., 2021. Reactive flows in porous media: challenges in theoretical and numerical methods. Annu. Rev. Chem. Biomol. 12, 543–571. https://doi.org/10.1146/annurev-chembioeng-092920-102703.

Ladd, A.J.C., Yu, L., Szymczak, P., 2020. Dissolution of a cylindrical disk in Hele-Shaw flow: a conformal-mapping approach. J. Fluid. Mech. 903, A46. https://doi.org/10.1017/jfm.2020.609.

Lake, L., Bryant, S., Araque-Martinez, A., 2002. Geochemistry and Fluid Flow. Elsevier, Amsterdam.

Li, L., Peters, C.A., Celia, M.A., 2006. Upscaling geochemical reaction rates using pore-scale network modeling. Adv. Water Res. 29, 1351–1370. https://doi.org/10.1016/j.advwatres.2005.10.011.

Lichtner, P.C., 1988. The quasi-stationary state approximation to coupled mass transport and fluid-rock interaction in a porous media. Geochim. Cosmochim. Acta 52, 143–165. https://doi.org/10.1016/0016-7037(88)90063-4.

Lichtner, P.C., Kang, Q., 2007. Upscaling pore-scale reactive transport equations using a multiscale continuum formulation. Water Resour. Res. 43, W12S15. https://doi.org/10.1029/2006WR005664.

Mehmani, Y., Sun, T., Balhoff, M., Eichhubl, P., Bryant, S., 2012. Multiblock pore-scale modeling and upscaling of reactive transport: application to carbon sequestration. Transp. Porous Med. 95, 305–326. https://doi.org/10.1007/s11242-012-0044-7.

Mikelić, A., Devigne, V., van Duijn, C.J., 2006. Rigorous upscaling of the reactive flow through a pore, under dominant Péclet and Damköhler numbers. SIAM J. Math. Anal. 38, 1262–1287. https://doi.org/10.1137/050633573.

Minde, M.W., Zimmermann, U., Madland, M.V., Korsnes, R.I., Schulz, B., Gilbricht, S., 2020. Mineral replacement in long-term flooded porous carbonate rocks. Geochim. Cosmochim. Acta 268, 485–508. https://doi.org/10.1016/j.gca.2019.09.017.

Molins, S., Soulaine, C., Prasianakis, N.I., Abbasi, A., Poncet, P., Ladd, A.J., Vitalii Starchenko, S.R., Trebotich, D., Tchelepi, H.A., Steefel, C.I., 2020. Simulation of mineral dissolution at the pore scale with evolving solid-fluid interfaces: Review of approaches and benchmark problem set. Comput.Geosci. 25, 1285–1318. https://doi.org/10.1007/s10596-019-09903-x.

Phillips, O.M., 1990. Flow-controlled reactions in rock fabrics. J. Fluid Mech. 212, 263–278. https://doi.org/10.1017/s0022112090001951.

Quintard, M., Whitaker, S., 1994a. Transport in ordered and disordered porous media II: generalized volume averaging. Transp. Porous Med. 14, 179–206. https://doi.org/10.1007/bf00615200.

Quintard, M., Whitaker, S., 1994b. Transport in ordered and disordered porous media III: closure and comparison between theory and experiment. Transp. Porous Med. 15, 31–49. https://doi.org/10.1007/bf01046157.

Rycroft, C.H., Bazant, M.Z., 2016. Asymmetric collapse by dissolution or melting in a uniform flow. Proc. Roy. Soc. Lond A 472, 20150531. https://doi.org/10.1098/rspa.2015.0531.

Shalev, E., Lyakhovsky, V., Yechieli, Y., 2006. Salt dissolution and sinkhole formation along the shore. J. Geophys. Res. 111, B03102. https://doi.org/10.1029/2005jb004038.

Soulaine, C., Roman, S., Kovscek, A., Tchelepi, H.A., 2017. Mineral dissolution and wormholing from a pore-scale perspective. J. Fluid Mech. 827, 457–483. https://doi.org/10.1017/jfm.2017.499.

Starchenko, V., Ladd, A.J.C., 2018. The development of wormholes in laboratory scale fractures: perspectives from three-dimensional simulations. Water Resour. Res. 54, 7946–7959. https://doi.org/10.1029/2018wr022948.

Starchenko, V., Marra, C.J., Ladd, A.J.C., 2016. Three-dimensional simulations of fracture dissolution. J. Geophys. Res. Solid Earth 121, 6421–6444. https://doi.org/10.1002/2016JB013321.

Szymczak, P., Ladd, A.J.C., 2013. Interacting length scales in the reactive-infiltration instability. Geophys. Res. Lett. 40, 3036–3041. https://doi.org/10.1002/grl.50564.

Whitaker, S., 1986. Flow in porous media I: A theoretical derivation of Darcy's law. Trans. Porous Med. 1, 3–25. https://doi.org/10.1007/bf01036523.